PAPER

Enhancing NiS performance: Na-doping for advanced photocatalytic and electrocatalytic applications†

V. G. Dileepkumar,‡[a,b,c] Swapna Pahra,‡[d,e] Nieves López-Salas, [ID] *[f]
B. M. Basavaraja, [ID] *[b] Afaq Ahmad Khan,[g] N. Sumanth,[a] Pooja Devi [ID] *[d,e] and
M. S. Santosh*[a,d]

Alkali metal doping is a new and promising approach to enhance the photo/electrocatalytic activity of NiS-based catalyst systems. This work investigates the impact of sodium on the structural, electronic, and catalytic properties of NiS. Comprehensive characterization techniques demonstrate that Na-doping causes significant changes in the NiS lattice and surface chemistry translating into a larger bandgap than NiS. Photocatalytic experiments demonstrate 98.5% degradation of 2,4-DCP under visible light, attributing it to improved light absorption and charge separation by Na–NiS nanoparticles. The effect of pH and pK_a on the degradation of 2,4-DCP has also been studied and reported. Additionally, electrochemical measurements of Na–NiS indicate overpotentials of 336 mV towards hydrogen evolution reaction (HER) and 350 mV towards oxygen evolution reaction (OER). The material's overall water splitting is found to be 2.61 V at a current density of 10 mA cm^{-2}. The results highlight the potential of Na–NiS as a versatile catalyst for environmental remediation and clean energy applications, paving the way for further exploration and optimization of doped transition metal sulfides.

1. Introduction

In recent years, wastewater treatment and clean energy production have become top priorities as the population's needs for freshwater and clean energy are increasing. Numerous researchers have initiated efforts to address this issue through the implementation of diverse methodologies. Among these, photocatalysis has emerged as a highly effective and successful approach for wastewater treatment.[1–3] On the other hand,

[a]*CSIR – Central Institute of Mining and Fuel Research (CIMFR), Digwadih Campus, Dhanbad - 828108, Jharkhand, India. E-mail: santoshms@cimfr.res.in*
[b]*Department of Chemistry (Science and Humanities), PES University, Bengaluru, India*
[c]*Department of Chemistry, HKBK College of Engineering, Bangalore - 560045, Karnataka, India*
[d]*Academy of Scientific and Innovative Research (AcSIR), Gaziabaad-201002, India. E-mail: poojaiitr@csio.res.in*
[e]*Materials Science and Sensor Applications, CSIR - Central Scientific Instruments Organisation (CSIO), Chandigarh-160030, India*
[f]*Paderborn University, Chemistry Department - Sustainable Materials Chemistry, Center for Sustainable Systems Design (CSSD), Warburger Strasse 100, 33098 Paderborn, Germany. E-mail: Nievesls@mail.uni-paderborn.de*
[g]*GreenCat Laboratory, Department of Chemical Engineering, Indian Institute of Technology (Indian School of Mines), Dhanbad – 826004, India*
†Electronic supplementary information (ESI) available. See DOI: https://doi.org/10.1039/d4nr04293j
‡These authors have contributed equally to this manuscript.

hydrogen, being classified as green energy and devoid of carbon emissions, is represented as a clean energy source. Moreover, hydrogen is the most practical propellant in a variety of applications such as fuel and electricity.[4,5] To produce hydrogen and cleanse wastewater, researchers have employed a wide range of substances, including carbon-based materials, MXenes, metal sulphides, metal oxides, and others.

Metal oxides have been extensively studied because of their wide bandgap, primarily attributed to the presence of the 2p oxygen orbitals. However, the hole carriers in metal oxides have a relatively high effective mass due to the confined nature of the oxygen 2p state, which is considered a disadvantage of oxides. Hence, a substantial amount of research has been directed toward the utilization of metal sulphides for diverse applications such as photocatalytic water treatment, electrocatalytic water splitting, membrane technology, and energy storage devices.[3,6–9] Yet, metal sulphides possess several drawbacks, such as the instability and recombination of charge carriers. Recent investigations have demonstrated that bimetallic sulphides have greater stability and can withstand higher temperatures. Further, the metallic sulphides that incorporate alkali metals in their complex structure have demonstrated great potential as a material for many applications such as photocatalysis, electrocatalysis, and energy storage. To address the limitations of metal sulphides, researchers have turned their attention towards doping these materials with various

other metals. Among the different dopants, particular interest is in the use of alkali metals. Introducing an alkali metal to the surface causes a substantial reduction in the number of defect states and promotes crystal growth, resulting in enhanced charge transport and increased catalytic characteristics of the material.[10–12]

The incorporation of heavy alkali metals, including potassium, rubidium, and caesium, can promote the development of larger grains with improved morphology and enhanced catalytic activity.[13] Conversely, alkali metals with small radiuses, including sodium and lithium, encounter challenges in maintaining a stationary position within the crystal. However, they are capable of unrestricted motion on the metal sulphide surface, an attribute that can potentially augment the catalytic activity. For instance, Naumov *et al.* (2006) investigated the luminescence and photoconduction properties of cadmium sulphide sheets doped with alkali metals.[10]

Apart from these, various other researchers have also incorporated alkali metals into metal sulphides *via* doping, which has been employed in various applications. In a more recent study, Bai *et al.* (2023) used copper sulphides doped with alkali metals as a new type of electrode for the oxygen evolution reaction with improved efficacy.[14]

In this work, we study the multifunctional properties of sodium-doped nickel sulfide (Na–NiS), focusing on its photocatalytic efficiency in degrading 2,4-DCP, a common industrial pollutant. Under visible light irradiation, Na–NiS achieved a degradation rate of 98.5%. To further proof the multifunctional nature of this material, we additionally studied the material performance in electrocatalytic water splitting, demonstrating significant enhancements in both the hydrogen evolution reaction (HER) and the oxygen evolution reaction (OER). Our findings position Na–NiS as a promising material for environmental remediation and clean energy production.

2. Experimental section

2.1. Synthesis of NiS and Na–NiS

A hydrothermal method was employed for the synthesis of NiS and Na–NiS. In the first step, $Ni(NO_3)_2 \cdot 6H_2O$ (1 mmol) was dissolved in Milli-Q water. L-cysteine (1 mmol) was added to this solution and stirred for 30 min. The resulting solution was then placed in an autoclave and subjected to a hydrothermal reaction for a period of 18 h at a temperature of 180 °C. The product obtained after the hydrothermal reaction was washed with ethanol to remove any impurities. The washed product was then dried in a desiccator overnight to ensure complete removal of any residual moisture. After drying, it was ground to a fine powder and stored for further use. The same procedure was followed to synthesize Na–NiS, with the addition of 5 wt% of $NaNO_3$ before the addition of L-cysteine.

2.2. Characterization of the materials

The crystal structures of the NiS and Na–NiS nanoparticles were analyzed using powder X-ray diffractometer (PXRD)

Bruker D8 Advance Eco X-ray diffractometer using graphite monochromatized Cu-Kα (λ = 1.54 Å) with a speed of 2° min^{-1} (10 to 80°), Ultraviolet–visible diffuse reflectance spectroscopy (UV-Vis DRS) studies were carried out using Shimadzu UV–vis 1800 double-beam spectrophotometer, Japan (200–900 nm), where the sample was placed on KBr powder for the analysis. X-ray photoelectron spectroscopic measurements were analyzed using XPS, PerkinElmer, MA, USA, PHI 5600 XPS, wherein the samples were initially pressed into a tablet form and dried overnight to remove any moisture content. The morphological studies were analyzed through TEM analysis using Thermofisher, Talos F200 S 200 kV, the samples were initially dispersed in ethanol and are then coated on a Cu grid for the analysis.

2.3. Photocatalytic studies

The degradation experiments were carried out using a 50 W LED (6000 K, 60 l m/w lumens, 97 × 65 mm size) as the visible light source. An external cooling jacket was used to avoid overheating and remove the excess heat. The pollutant concentration was varied by adding the required amount from the stock solution (1 g L^{-1}) into 95 mL of Millipore water taken in a glass reactor. A variable amount (10 to 100 mg) of the photocatalyst was added to the pollutant solution. The pH of the pollutant solution was varied using 0.1 M NaOH/HCl. The solution containing the pollutant and the catalyst was placed in a custom-built reactor (21 cm length from the solution to the light source) for the degradation studies. 2 mL of the solution was withdrawn at regular intervals to study the degradation of pollutants. Scavenging experiments were performed to study the reactive oxygen species (ROS) during the photocatalytic reaction, where sodium nitride, potassium iodide and methanol were used as the singlet oxygen ($^1O_2$), hole (h$^+$), and as the hydroxyl (˙OH) radical scavengers, respectively.

2.4. Electrochemical studies

The electrochemical performance of the prepared electrodes OER, HER and overall water splitting was investigated using a Metrohm Autolab PGSTAT302N electrochemical workstation. The experiments were run in a three-electrode single-compartment setup using a glassy carbon electrode (GCE) as the working electrode, a graphite rod as the counter electrode, and Ag/AgCl as the reference electrode. HER performance was examined *via* linear sweep voltammetry (LSV) in the potential range from 0 to −0.95 V *vs.* RHE with a scan rate of 5 mV s^{-1} in 1.0 M aqueous KOH electrolyte. Similarly, OER was studied in 1.0 M KOH in a potential range of 0 to 2.0 V *vs.* RHE and overall water splitting from 0 to 3.0 V *vs.* RHE at a scan rate of 5 mV s^{-1}. Electrochemical impedance spectroscopy measurements were also carried out in the frequency range 10 kHz to 0.1 Hz with an AC signal of amplitude 0.01 Vrms. The stability of the electrodes was assessed *via* chronopotentiometry measurement at room temperature for 12 h. All potentials were converted to the potential on the reversible hydrogen electrode (RHE) scale using eqn (1) given below.

$$E_{RHE} \text{ (V)} = E_{Ag/AgCl} + 0.0591 \times pH + 0.197 \text{ (V)} \qquad (1)$$

The electrochemical active surface area (ECSA) can also be computed by using the equation

$$\text{ECSA} = C_{dl}/C_s \tag{2}$$

where C_{dl} is double-layer capacitance and C_s is specific capacitance.

The following equation was used to get the turnover frequency (TOF) value:

$$\text{TOF} = \frac{1}{2} \times F \times n \tag{3}$$

where n is the number of active sites and F is the Faraday constant (96485 C mol^{-1})

The integrated charge (Q_{cv}) obtained from the CV measurement, which is directly proportional to n, which can be determined by using the following equation.[15–17]

$$n = Q_{cv}/2F \tag{4}$$

The theoretical hydrogen generation can be determined using chronopotentiometry at a constant current of 10 mA cm^{-2} for 12 h using the faradaic efficiency formula given below.

$$\text{FE}\% = \frac{\text{No. of moles of hydrogen produced}}{\text{Charge}/2F} \tag{5}$$

3. Results and discussion

3.1. Structural analysis of NiS and Na–NiS

PXRD analysis of bare NiS and Na–NiS are shown in Fig. 1a. The obtained PXRD peaks confirm the successful formation of NiS, which is in accordance with the reported JCPDS card no. 002-9313. The reduction in the intensity of (011) and (012) NiS peaks in the PXRD spectra of Na–NiS indicates the successful doping of Na into the NiS matrix. The planes (121), (013), (132), (233), and (163) suggest that Na is present as Na$_2$S$_4$ in Na–NiS, as confirmed by the planes that match well with the JCPDS card no. 000-2586. The crystallite size of NiS and Na–NiS was calculated using Debye–Scherrer's equation, and the resulting sizes are given in Table 1. It is clear from Table 1 that the crystallite sizes of Na-NiS are much smaller compared with the NiS sample.

The effect of sodium doping on the optical properties of the material was studied using UV-Vis DRS. The absorption spectra of the synthesized NiS and Na–NiS are shown in Fig. 1b. Both materials show two absorption bands at 224 nm and 354 nm, which is a typical NiS behavior, as reported in literature.[18] The bandgap of NiS and Na–NiS was calculated using the Kubelka–Munk (K–M) function, and the data are shown in Fig. 1c. From the K–M function, the bandgap was estimated to be 1.10 eV and 1.3 eV for NiS and Na–NiS, respectively. Thus, indicating that the incorporation of Na onto NiS nanoparticles has a significant impact on the electron transport properties of the material. The increase in the bandgap
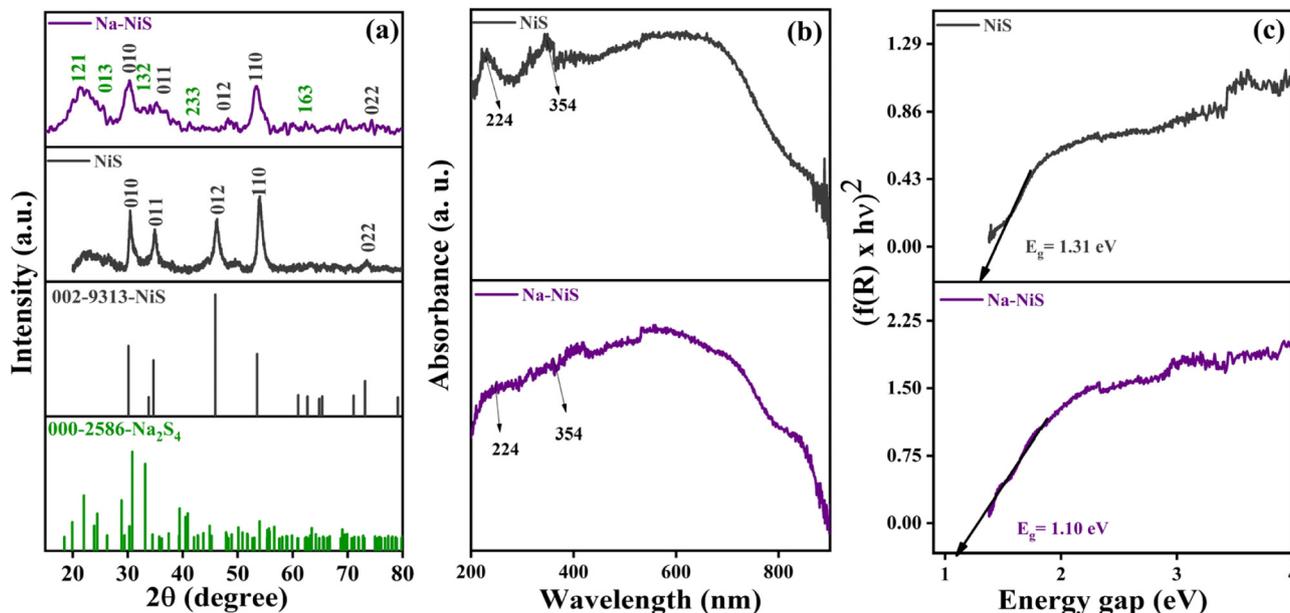

Fig. 1   (a) PXRD spectra of bare NiS and Na-doped NiS (Na–NiS) confirming NiS formation. The reduced intensity of NiS peaks {(011) and (012)} and the appearance of Na$_2$S$_4$ peaks {(121), (013), (132), (233), (163)} indicate the successful doping of Na; (b) absorption spectra of synthesized NiS and Na–NiS showing two characteristic absorption bands at 224 nm and 354 nm, consistent with typical NiS behavior; (c) UV-Vis DRS analysis showing bandgap increase from 1.10 eV (NiS) to 1.3 eV (Na–NiS) due to sodium doping, affecting electron transport properties.

also supports the reduction in the PXRD intensity observed in Fig. 1c caused by the introduction of Na onto the NiS lattice.[19]

The XPS spectra of Ni 2p and S 2p signals of NiS and Na–NiS are shown in Fig. 2. The two predominant states of Ni 2p are present in the NiS nanoparticles, which are Ni $2P_{3/2}$ and Ni $2P_{1/2}$ observed at 853.4 eV and 870.5 eV, respectively.[20] These states were further deconvoluted into Ni^{3+} and Ni^{2+} and their respective satellite peaks. The Ni^{3+} and Ni^{2+} states can be confirmed by the presence of deconvoluted peaks at 853.4 eV and 855.9 eV for Ni $2P_{3/2}$, 870.5 eV and 873.56 eV for Ni $2P_{1/2}$, respectively.[21,22] In the case of Na–NiS, the peaks observed for Ni $2P_{3/2}$, Ni $2P_{1/2}$, and the deconvoluted peaks shift slightly towards a higher binding energy level. This could be attributed to the Na doping, as smaller Na atoms would induce a contraction in the volume of NiS, leading to alterations in its chemical bonding.[23] The S 2p oxidation state can be observed in Fig. 2b, in which S exists in the form of $2p_{3/2}$, $2p_{1/2}$, and S^{2-} observed at 162.07 eV, 163.20 eV, and 164.33 eV, respectively.[24] The other peak observed at 168.58 eV could be due to the surface oxidation of S to sulfate. Further, the Na 1s peak at 1070.8 eV shown in Fig. 2c confirms the presence of Na in the Na–NiS nanoparticles.

3.2. Morphological analysis

The morphological analysis of the synthesized NiS and Na–NiS nanoparticles, including crystallinity and elemental distri-

Table 1 Calculated crystallite size of NiS and Na–NiS nanoparticles using Debye–Scherrer's equation

Plane	Crystallite size (nm)	
	NiS	Na–NiS
010	18.2	11.59
011	23.8	22.67
012	12.2	17.67
110	22.2	18.23
022	24.7	13.51

bution, was carried out using TEM, SAED and STEM-EDS mapping. As illustrated in Fig. 3, both NiS (a and b) and Na–NiS (d and e) nanoparticles exhibit spherical-like morphologies, indicative of uniform particle formation. The spherical shape of the nanoparticles suggests that the synthesis method effectively controlled the nucleation and growth processes, leading to the formation of particles with consistent shapes and sizes. The crystallinity of the NiS and Na–NiS nanoparticles was confirmed through SAED patterns, shown in Fig. 3c and 3f. The diffraction rings observed in the SAED patterns correspond to the polycrystalline nature of both NiS and Na–NiS nanoparticles. HAADF imaging combined with STEM-EDS mapping was employed to assess the elemental composition and distribution within the nanoparticles. For NiS nanoparticles, the STEM-EDS mapping results, depicted in Fig. 3g–i, clearly show the presence of Ni and S elements uniformly distributed throughout the nanoparticles. In contrast, the analysis of Na–NiS nanoparticles, shown in Fig. 3j–l, not only confirms the presence of Ni and S but also reveals the successful incorporation of Na into the NiS matrix.

3.3. Photocatalytic degradation of 2,4-dichlorophenol

To evaluate the impact of Na metal doping on the photocatalytic performance, both the undoped material (NiS) and the Na-doped NiS (Na–NiS) nanoparticles were subjected to photocatalytic degradation studies using 2,4-dichlorophenol (2,4-DCP) as the target pollutant. The results revealed a significant difference in their performances: NiS achieved a degradation efficiency of 67.1%, while Na–NiS demonstrated a remarkable improvement, achieving 98.5% degradation under visible light (Fig. 4). In the absence of light, Na–NiS catalyst led to a modest 10% degradation of 2,4-DCP, likely due to the adsorption of the pollutant onto the catalyst's surface (Fig. 4a).

For a better understanding of the catalytic properties of the catalyst and to identify the inorganic radicals responsible for the degradation, several studies were conducted. These studies
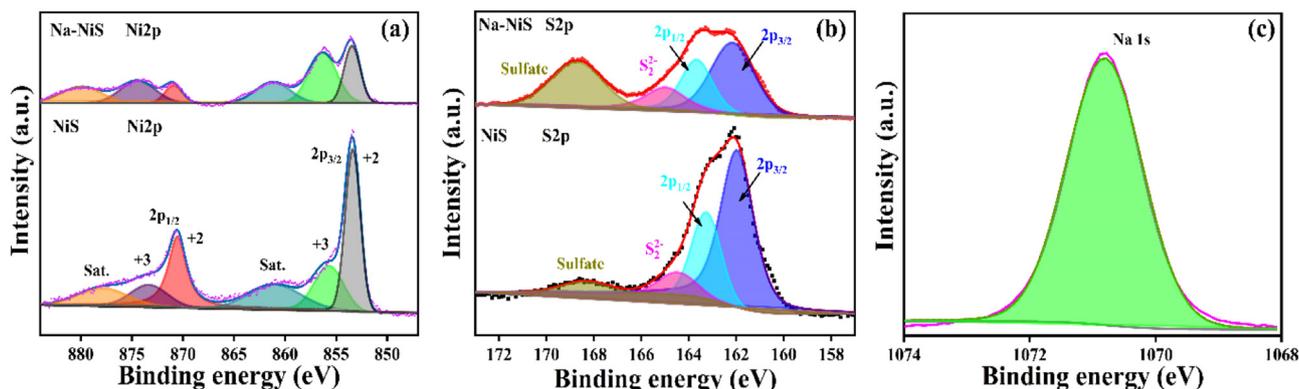

Fig. 2 (a) XPS spectra of Ni 2p states in NiS and Na–NiS, showing Ni $2P_{3/2}$ and Ni $2P_{1/2}$ at 853.4 eV and 870.5 eV, respectively, with deconvoluted Ni^{3+} and Ni^{2+} states. Sodium doping causes a shift to higher binding energies, indicating increased conduction of electrons and elevated Fermi energy; (b) XPS spectra of the S 2p oxidation state showing S $2p_{3/2}$, S $2p_{1/2}$, and S^{2-} peaks at 162.07 eV, 163.20 eV, and 164.33 eV, respectively; (c) XPS spectra showing the Na 1s peak at 1070.8 eV, confirming the presence of Na in the Na–NiS nanoparticles.
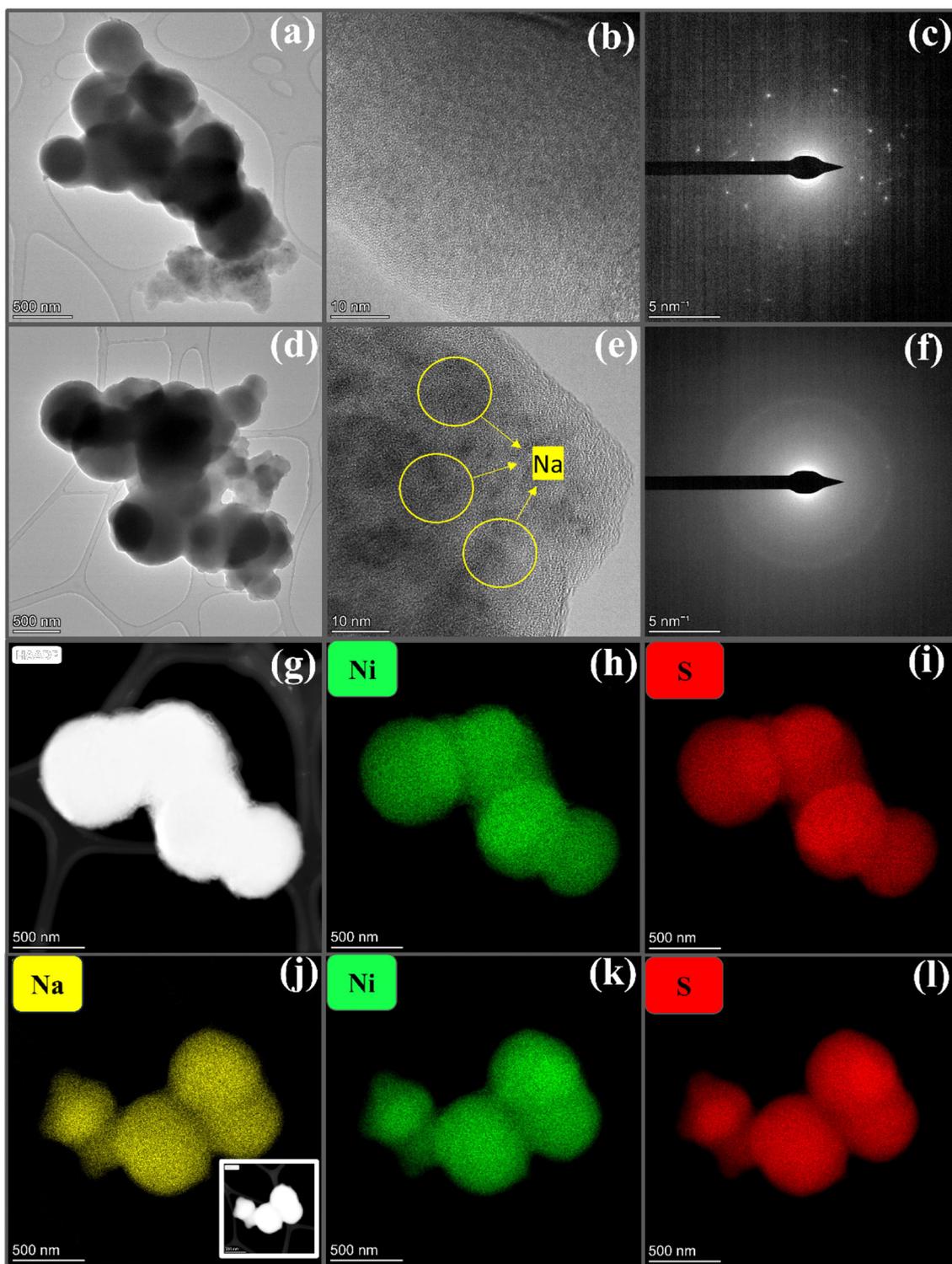
Fig. 3 (a and b) and (d and e) TEM micrographs of NiS and Na–NiS nanoparticles exhibiting spherical morphologies and uniform particle formation; (c and f) SAED patterns of NiS and Na–NiS nanoparticles confirming the polycrystalline nature of the nanoparticles; (g–i) and (j–l) HAADF STEM-EDS mapping of NiS and Na–NiS showcasing uniform distribution of Ni and S in NiS and successful incorporation of Na in Na–NiS, respectively.
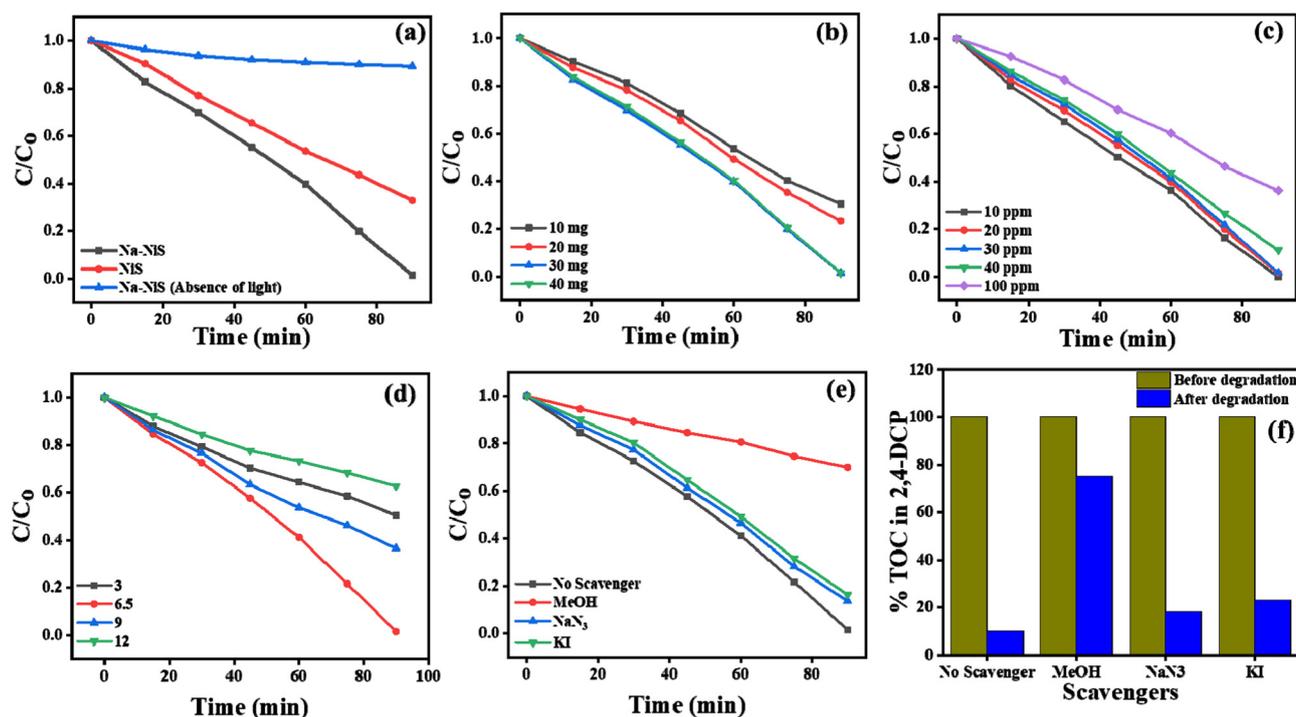
Fig. 4 (a) Effect of light and prepared catalysts (NiS and Na–NiS) on the removal of 2,4-DCP; (b) degradation of 2,4-DCP using various concentrations of Na–NiS; (c) effect of Na–NiS on the degradation of 2,4-DCP at various concentrations; (d) effect of acidic, neutral and basic pH on the removal of 2,4-DCP by Na–NiS; (e) trapping experiments to understand the effect of inorganic radicals on the removal of 2,4-DCP; (f) % TOC remaining after trapping experiments.

included analyzing changes in pollutant concentration, catalyst concentration, pH variation, and radical analysis.

3.3.1. Effect of concentration of the catalyst, pollutant, and pH on the degradation of 2,4-DCP using Na–NiS. At first, the concentration of 2,4-DCP (20 ppm) was kept constant while the catalyst concentration was varied from 10 to 40 mg (Fig. 4b). This was performed to understand the photocatalytic ability of the catalyst. During the photocatalytic degradation reactions, 69.6%, 76.7%, 98.5% and 98.4% degradations were observed for catalyst concentrations of 10 mg, 20 mg, 30 mg and 40 mg, respectively. The results showed that degradation increased with an increase in the catalyst concentration but reached a plateau at concentrations above 30 mg, which can be attributed to the blocking of light due to dispersion at higher concentrations.[25]

Another experiment was carried out to understand the degradation capabilities of the catalyst by varying the concentration of 2,4-DCP from 10 to 100 ppm, while keeping the catalyst concentration constant at 30 mg (Fig. 4c). The results showed that at higher concentrations, the degradation rate was reduced. As the concentration of pollutants increases, more active sites of the catalyst are required for degradation.[26] However, since the concentration of the catalyst remains constant, only a minimal number of active sites will be available. The degradation was shown to be 88.7% and 63.75% when the concentration of 2,4-DCP was increased to 40 ppm and 100 ppm, respectively. However, even at these concentrations, the catalytic properties of the Na–NiS were notable.

pH plays a major role when it comes to practical pollutant degradation. According to several studies, an acidic medium is known to potentially enhance pollutant degradation due to its ability to inhibit the recombination of ˙OH radicals present in water, which in turn increases its oxidation potential.[27,28] To understand the pH effect on the degradation of 2,4-DCP by the catalyst, the pH was varied from acidic to basic (pH of 3 to 12) (Fig. 4d). Interestingly, higher degradation was observed in neutral pH. When the pH was changed to acidic or basic, the degradation decreased drastically.

The pK_a value of 2,4-DCP is 7.89, which means that at a pH close to this value, the molecule is only slightly ionized.[29] When the pH is below the pK_a, 2,4-DCP primarily exists in its protonated or non-ionized form. As the pH rises above the pK_a, the molecule exits mainly in its anionic form.[30] Non-ionized molecules are generally more hydrophobic, which enhances their interaction with hydrophobic regions of catalyst surfaces. This increased adsorption leads to higher degradation rates. The anionic form is more water-soluble and less likely to adsorb onto the catalyst surface due to electrostatic repulsion.[31] This reduced adsorption can lead to lower degradation efficiency.

Several reports have been reported that 2,4-DCP requires more time for the degradation, here the synthesised material has degraded 2,4-DCP in about 90 min, which shows the effect of Na doping on the NiS catalyst. For a better understanding of the effect of different catalysts on 2,4-DCP removal, a compari-

Table 2 Comparison table for the removal of 2,4-DCP with existing catalysts

Catalyst	Light source	% degradation	Time	Ref.
Ag/AgBr	UV	89.39%	5 h	32
ZnS	UV	53%	120 min	33
CuFeS$_2$	Visible light	90%	120 min	34
CuS@CNs	UV	90%	2.5 h	35
N–rGO@AgInS$_2$	Visible light	95%	7 h	36
In$_2$O$_3$/ZnIn$_2$S$_4$	Visible light	95%	120 min	37
NiS	**Visible light**	**67.1%**	**90 min**	**This study**
Na–NiS	**Visible light**	**98.5%**	**90 min**	**This study**

son with the reported data is given in Table 2. Hence, it can be said that the Na doped NiS catalyst can be used as a photo-catalyst for the degradation of organic pollutants.

3.3.2. Photodegradation of 2,4-DCP by trapping experiments. To understand the radicals responsible for the degradation, trapping experiments were carried out for the removal of 2,4-DCP at real pH. The results of the trapping experiments are shown in Fig. 4e. The addition of a ˙OH radicals scavenger caused a significant reduction in the degradation of 2,4-DCP from 98.5% to 30.1%. Upon the addition of an h$^+$ scavenger, a minimal decrease in degradation (86.44%) was observed, and the ^{1}O$_2$ scavenger also led to a negligible decrease in degradation (83.7%). These findings suggest that the degradation of 2,4-DCP was mainly due to the ˙OH radicals, while holes and singlet oxygen had a minimal impact. Further, to confirm the presence large number of hydroxyl radicals, an alternative method was employed. In a specific experiment, 30 mg of the sample was dispersed in a coumarin solution and subjected to light irradiation. At regular intervals of 15 min, a 2 mL aliquot was withdrawn and analysed using photoluminescence (PL) studies. The results from the PL analysis showed a progressive increase in the fluorescence intensity, indicating the formation of a large number of hydroxyl radicals under the given conditions (Fig. S2a†). Additionally, to evaluate the absence of singlet oxygen, EPR spectroscopy was performed and the results are presented in Fig. S2b.† The EPR spectra revealed no noticeable change in the intensity, clearly demonstrating the absence of singlet oxygen in the system. These findings collectively confirm the generation of hydroxyl radicals during the reaction while ruling out the contribution of singlet oxygen.

The total organic carbon (TOC) analysis provides valuable information about the removal of 2,4-DCP from the solution. Fig. 4f shows that after the addition of methanol, 75% of the carbon content remained, indicating that only 25% of the 2,4-DCP was degraded. This suggests that methanol hinders the formation of hydroxyl radicals, leading to a reduced degradation efficiency of the catalyst. In contrast, after the addition of NaN$_3$ and potassium iodide (KI), the remaining carbon content decreased significantly to 18% and 23%, respectively. These results indicate that the material generates more hydroxyl radicals compared to holes and singlet oxygen, further underscoring the importance of hydroxyl radicals in the degradation process.

3.4. Electrocatalytic performance of the catalysts

The electrocatalytic performance of both the NiS and Na–NiS loaded onto the glassy carbon electrode (GCE) was examined for HER and OER. Fig. 5a shows the LSV curves at a scan rate of 5 mV s^{-1}. In HER, The NiS and Na–NiS samples had the lowest driving potential of 336 mV to reach a current density of 10 mA cm^{-2}, which is 110 mV lower than that of NiS. Similarly, for OER, NiS and Na–NiS showed an overpotential of 630 mV and 350 mV, respectively (Fig. 5d). Electrochemical impedance spectroscopy (EIS) measurements were carried out to further study the charge transfer properties at the electrode/electrolyte interface and the outcomes are displayed in Fig. 5b–e. In the Nyquist plot for HER, it can be seen that the charge transfer resistance (R_{ct}) of Na–NiS is lower (0.0484 kΩ) than NiS (5.79 kΩ). Likewise, in OER, it showed a charge resistance of 0.0702 kΩ and 0.098 kΩ for Na–NiS and NiS, respectively. The lower R_{ct} values for Na–NiS than NiS in both cases verify the enhanced charge transfer due to the doping of Na into NiS.

The catalytic reaction kinetics was also investigated using Tafel slope measurements. As shown in Fig. 5c and 5f, the Tafel plots for the electrodes were determined to be 246 and 192 mV dec^{-1} in HER and 678 and 379 mV dec^{-1} in OER for NiS and Na–NiS, respectively. This clearly states that Na doping into NiS to form Na–NiS possesses a significantly enhanced catalytic performance than NiS alone. The observed HER and OER performance of NiS and Na–NiS is compared with some existing sulphur-based catalysts (Table 3). From the table it is clear that the prepared material exhibits better electrocatalytic activity towards both HER and OER compared to most of the literature highlighting the importance of the Na doping on NiS catalyst.

Also, Fig. S3a–c† show that the catalyst possesses remarkable stability in both positive and negative constant current density of 10 mA cm^{-2} for around 12 h with a slight change in electrocatalytic performance (Fig. S3b–d†).

To better understand the amount of accessible active sites on NiS and Na–NiS, the electrochemical surface area (ECSA) was also computed using eqn (2). The C_{dl} was determined for both materials by recording cyclic voltammograms at different scan rates (20, 40, 80, 100, 120, and 140 mV sec^{-1}) in a non-faradaic region. The C_{dl} for NiS and Na–NiS was calculated to be 0.038 mF cm^{-2} and 2.09 mF cm^{-2}, respectively (Fig. S3e†). The
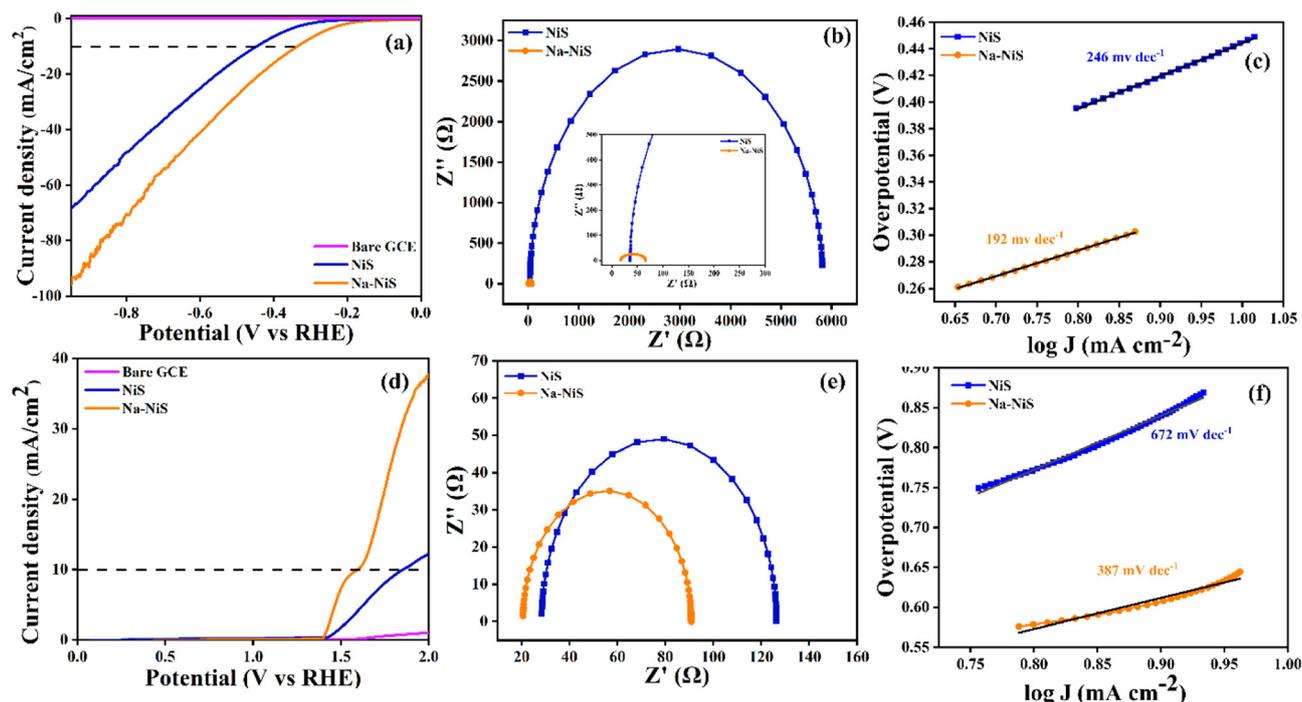
Fig. 5 HER and OER performance of NiS and Na–NiS catalysts; (a and d) HER shows a significantly lower driving potential to reach a current density of 10 mA cm^{-2} for Na–NiS compared to NiS, while OER polarisation curves for Na–NiS exhibit a markedly reduced overpotential compared to NiS; (b and e) Nyquist plots for NiS and Na–NiS during HER and OER, where the charge transfer resistance (R_{ct}) at the electrode/electrolyte interface is significantly lower for Na–NiS in both reactions; (c and f) Tafel slope measurements for NiS and Na–NiS during HER and OER demonstrate improved catalytic performance for Na–NiS over NiS.

Table 3 Comparative table of HER and OER performance by sulfur-based catalyst with existing literature

Catalyst	Electrolyte	Overpotential (mV)		Tafel slope (mv dec^{-1})		
		HER@mA cm^{-2}	OER@mA cm^{-2}	HER	OER	Ref.
Phosphorene quantum dots/MoS$_2$	0.1 M KOH	600@10	370@10	162	46	39
MoS$_2$/NiCoS	1 M KOH	189@10	290@10	75	77	40
Co$_3$S$_4$@MoS$_2$–Ni$_3$S$_2$	1 M KOH	136@10	270@50	72	69	41
Co$_3$O$_4$@MoS$_2$	1 M KOH	205@10	230@20	98	45	42
MoS$_2$/NiS	1 M KOH	244@10	350@10	97	108	43
NiS	**1 M KOH**	**336@10**	**630@10**	**246**	**678**	**This study**
Na–NiS	**1 M KOH**	**110@10**	**350@10**	**192**	**379**	**This study**

respective CVs at different scan rates for both NiS and Na–NiS are shown in Fig. S4.†

The specific capacitance of a material is measured on an atomically smooth planar surface under the same electrolyte conditions. In the present work, it was not possible to measure the C_s, as C_{dl} is directly proportional to ECSA; hence, on this basis, it can be concluded that Na–NiS possess larger ECSA than NiS.[38]

The number of hydrogen molecules that evolve on an active site over time, or turnover frequency (TOF) per active site, was calculated using eqn (3) in order to further explore the intrinsic chemical characteristics of the material. The number of active sites (n) was calculated from the CV data in the potential range of 0.427 to 0.566 V $vs.$ RHE at a scan rate of 20 mV s^{-1}.

The integrated charge (Q_{cv}) obtained from the CV measurement, which is directly proportional to n, can be determined by using eqn (4). Accordingly, the TOF for Na–NiS was calculated to be 0.073 s^{-1}, 0.037 s^{-1} in HER and OER, respectively.

The HER and OER activities of the Na–NiS electrode were evaluated for overall water splitting using the equivalent Na–NiS electrodes as anode and cathode. The results obtained (HER‖OER at Na–NiS anode and Na–NiS cathode, respectively) show a reasonably exceptional catalytic activity on total water electrolysis (Fig. S5a†). In this case, the cell voltage attained to drive the 10 mA cm^{-2} current density was 2.61 V.

Finally, to test the stability of the Na–NiS catalyst for HER and OER, chronopotentiometry measurements were performed in 1.0 M KOH aqueous electrolyte at an applied bias of 10 mA

cm^{-2} for 12 h (Fig. S5b†), which showed only a slight decrease in performance (Fig. S5c†).

The number of moles of hydrogen produced by Na–NiS were 0.186 mmol h^{-1} according to eqn (5). The lower overpotential for HER of Na–NiS (336 mV *vs.* 446 mV for NiS) and OER (350 mV *vs.* 630 mV for NiS) and the lower charge transfer resistance and improved catalytic kinetics, evidenced by Tafel slope and electrochemical impedance spectroscopy, indicate the enhanced electron transfer due to Na doping. Na–NiS also showed remarkable stability and efficiency in overall water splitting, highlighting its potential as an effective catalyst for hydrogen generation.

The catalyst's recyclability and stability were studied by subjecting Na–NiS to post HER and OER cyclic studies using HRTEM and PXRD. The obtained results are presented in Fig. S6 and S7.† The HRTEM analysis provides clear evidence of the catalyst's stability after undergoing multiple HER and OER cycles. The microstructural features of Na–NiS remained intact, demonstrating its stability under electrocatalytic conditions. HAADF imaging further confirmed the retention of key elements (Na, Ni & S) within the Na–NiS sample, indicating no significant elemental loss or degradation. Further, EDAX revealed the presence of oxygen in the post-cycled sample. This may most likely be attributed to surface oxidation that occurred during the HER and OER processes, which is a common phenomenon under electrocatalytic conditions due to the exposure of the electrolyte and reactive intermediates.

Additionally, the PXRD analysis corroborated these findings by showing that the characteristic diffraction peaks corresponding to Na–NiS were preserved even after the completion of HER and OER studies. This retention of the crystalline structure strongly validates the structural integrity and stability of the Na–NiS catalyst, making it a reliable catalyst for long-term electrocatalytic applications.

4. Conclusions

The successful synthesis of Na-doped NiS nanoparticles was carried out by a simple hydrothermal method. The decreased intensity observed in the PXRD spectra was attributed to the doping of Na onto the NiS lattice. The Na–NiS had shown a reduced bandgap of 1.10 eV compared to 1.31 eV by NiS nanoparticles. The morphological analysis represents a spherical-like morphology, and the STEM-EDS mapping confirms the presence of Na in the NiS lattice. The catalytic properties of Na–NiS were greatly enhanced compared to NiS. In the photocatalytic degradation of pollutants, Na–NiS exhibited a very high 2,4-DCP degradation efficiency of 98.5% at close to neutral pH (6.5), indicating a degradation pathway involving ˙OH radicals, confirmed by trapping experiments. As an electrocatalyst, Na–NiS showed lower overpotential for HER and OER than its non-doped counterpart and exceptional catalytic activity towards overall water splitting.

References

1 T. Ahamad, M. Naushad, Y. Alzaharani and S. M. Alshehri, *J. Mol. Liq.*, 2020, **311**, 113339.
2 G. S. Das, J. P. Shim, A. Bhatnagar, K. M. Tripathi and T. Y. Kim, *Sci. Rep.*, 2019, **9**(1), 15084.
3 M. Ghobadifard, G. Feizi and S. Mohebbi, *Appl. Organomet. Chem.*, 2022, **36**(12), e6911.
4 S. R. Khaladkar, O. Maurya, G. Gund, B. Sinha, G. Kamble, J. H. Kim, R. R. Deshmukh and A. Kalekar, *Mater. Adv.*, 2024, **5**, 4345–4353.
5 V. Navakoteswara Rao, P. Ravi, M. Sathish, N. Lakshmana Reddy, K. Lee, M. Sakar, P. Prathap, M. Mamatha Kumari, K. Raghava Reddy, M. N. Nadagouda, T. M. Aminabhavi and M. V. Shankar, *J. Hazard. Mater.*, 2021, **413**, 125359.
6 L. Chen, H. Jang, M. G. Kim, Q. Qin, X. Liu and J. Cho, *Nanoscale*, 2020, **12**, 13680–13687.
7 Q. Wu, D. Lu, K. Kumar Kondamareddy, W. Ho, D. Cao, Y. Zeng, B. Zhang, Y. Zhang, L. Xie, B. Zhao, Z. Wang, H. Hao, H. Fan and H. Wang, *Arabian J. Chem.*, 2022, **15**(3), 103689.
8 B. Zhou, J. Song, C. Xie, C. Chen, Q. Qian and B. Han, *ACS Sustainable Chem. Eng.*, 2018, **6**, 5754–5759.
9 S. Kumar, A. P. Singh, C. Bera, M. Thirumal, B. R. Mehta and A. K. Ganguli, *ChemSusChem*, 2016, **9**, 1850–1858.
10 A. V. Naumov, T. G. Bolgova, V. N. Semenov, T. L. Maiorova and V. G. Klyuev, *Inorg. Mater.*, 2006, **42**, 463–469.
11 Y. Wang, Y. Liu, X. Shi, L. Huang, J. Tong, G. Wang and D. Pan, *New J. Chem.*, 2021, **45**, 14158–14166.
12 E. Khorashadizade, S. Mohajernia, S. Hejazi, H. Mehdipour, N. Naseri, O. Moradlou, N. Liu, A. Z. Moshfegh and P. Schmuki, *ChemElectroChem*, 2020, **7**, 1699–1706.
13 T. Y. Lin, C. H. Chen, L. W. Wang, W. C. Huang, Y. W. Jheng and C. H. Lai, *Nano Energy*, 2017, **41**, 697–705.
14 C. Bai, Y. Wu, Y. Xin, J. Mou, L. Xia, D. Ding, X. Zheng and P. Yu, *J. Alloys Compd.*, 2023, **962**, 171171.
15 S. B. Roy, K. Akbar, J. H. Jeon, S. K. Jerng, L. Truong, K. Kim, Y. Yi and S. H. Chun, *J. Mater. Chem. A*, 2019, **7**, 20590–20596.

16 D. H. Kweon, M. S. Okyay, S. J. Kim, J. P. Jeon, H. J. Noh, N. Park, J. Mahmood and J. B. Baek, *Nat. Commun.*, 2020, **11**(1), 1278.

17 S. Anantharaj, P. E. Karthik and S. Noda, *Angew. Chem., Int. Ed.*, 2021, **60**, 23051–23067.

18 M. Salavati-Niasari, G. Banaiean-Monfared, H. Emadi and M. Enhessari, *C. R. Chim.*, 2013, **16**, 929–936.

19 M. Khatun, P. Mitra and S. Mukherjee, *Hybrid Adv.*, 2023, **4**, 100079.

20 T. Liu, C. Jiang, B. Cheng, W. You and J. Yu, *J. Mater. Chem. A*, 2017, **5**, 21257–21265.

21 Z. Chen, Y. Gao, F. Chen and H. Shi, *Chem. Eng. J.*, 2021, **413**, 127474.

22 I. H. Kwak, H. S. Im, D. M. Jang, Y. W. Kim, K. Park, Y. R. Lim, E. H. Cha and J. Park, *ACS Appl. Mater. Interfaces*, 2016, **8**, 5327–5334.

23 S. Xiang, W. Li, Y. Wei, J. Liu, H. Liu, L. Zhu, S. Yang and H. Chen, *iScience*, 2019, **15**, 156–164.

24 Y. Lin, Z. Qiu, D. Li, S. Ullah, Y. Hai, H. Xin, W. Liao, B. Yang, H. Fan, J. Xu and C. Zhu, *Energy Storage Mater.*, 2018, **11**, 67–74.

25 V. G. Dileep Kumar, S. Kumari, K. R. Balaji, A. Ahmad Khan, C. R. Ravikumar, B. M. Basavaraja, M. S. Santosh and S. Rtimi, *Chem. Eng. J.*, 2023, **462**, 142187.

26 V. G. Dileepkumar, K. R. Balaji, R. Vishwanatha, B. M. Basavaraja, S. Ashoka, I. M. Al-Akraa, M. S. Santosh and S. Rtimi, *Chem. Eng. J.*, 2022, **446**, 137023.

27 A. V. Mohod, A. C. S. C. Teixeira, M. V. Bagal, P. R. Gogate and R. Giudici, *J. Environ. Chem. Eng.*, 2023, **11**, 109773.

28 W. Huang, Y. Huang, S. Wang, H. Lin and G. Mailhot, *Processes*, 2021, **9**, 1–18.

29 V. G. D. Kumar, K. R. Balaji, R. Viswanatha, G. Ambika, R. Roopa, B. M. Basavaraja, M. Chennabasappa, C. R. R. Kumar, Z. Chen, X. T. Bui and M. S. Santosh, *Chemosphere*, 2022, **287**, 132174.

30 J. Yu, T. Wang and S. Rtimi, *Appl. Catal., B*, 2019, **254**, 66–75.

31 H. Jia and C. Wang, *Chem. Eng. J.*, 2012, **191**, 202–209.

32 M. M. Moja, A. B. Mapossa, E. M. N. Chirwa and S. Tichapondwa, *Environ. Sci. Pollut. Res.*, 2024, **31**, 11857–11872.

33 X. Lv, Y. Wang, Y. Wang and Z. Lin, *J. Nanosci. Nanotechnol.*, 2016, **16**, 1060–1066.

34 X. Xu, D. Tang, J. Cai, B. Xi, Y. Zhang, L. Pi and X. Mao, *Appl. Catal., B*, 2019, **251**, 273–282.

35 Y. Chen, R. Su, F. Wang, W. Zhou, B. Gao, Q. Yue and Q. Li, *Chemosphere*, 2021, **270**, 129295.

36 A. Tadjarodi, A. Hossein, C. Khavar and M. Imani, *Curr. Chem. Lett.*, 2013, **2**, 77–84.

37 Q. Zhu, Y. Sun, S. Xu, Y. Li, X. Lin and Y. Qin, *J. Hazard. Mater.*, 2020, **382**, 121098.

38 C. C. L. McCrory, S. Jung, J. C. Peters and T. F. Jaramillo, *J. Am. Chem. Soc.*, 2013, **135**, 16977–16987.

39 R. Prasannachandran, T. V. Vineesh, M. B. Lithin, R. Nandakishore and M. M. Shaijumon, *Chem. Commun.*, 2020, **56**, 8623–8626.

40 C. Qin, A. Fan, X. Zhang, S. Wang, X. Yuan and X. Dai, *J. Mater. Chem. A*, 2019, **7**, 27594–27602.

41 A. Muthurasu, G. P. Ojha, M. Lee and H. Y. Kim, *Electrochim. Acta*, 2020, **334**, 135537.

42 J. Liu, J. Wang, B. Zhang, Y. Ruan, H. Wan, X. Ji, K. Xu, D. Zha, L. Miao and J. Jiang, *J. Mater. Chem. A*, 2018, **6**, 2067–2072.

43 S. Guan, X. Fu, Z. Lao, C. Jin and Z. Peng, *Sustainable Energy Fuels*, 2019, **3**, 2056–2066.